Multifunctional Nanoparticles

DOI: 10.1002/anie.201101447

Facile Preparation of Multifunctional Upconversion Nanoprobes for Multimodal Imaging and Dual-Targeted Photothermal Therapy**

Liang Cheng, Kai Yang, Yonggang Li, Jianhua Chen, Chao Wang, Mingwang Shao, Shuit-Tong Lee, and Zhuang Liu**

The rapid development in nanotechnology has allowed the engineering of various functional nanomaterials with multiple discrete function-related components integrated in one nanoparticle for applications in multimodality biomedical imaging to circumvent the limitations of each single imaging mode.[1–4] Upconversion nanoparticles (UCNPs), particularly lanthanide-doped rare-earth nanocrystals, which are able to emit high-energy photons under excitation by near-infrared (NIR) light, have found potential applications in many different fields, including biomedicine.[5–8] In the past few years, UCNPs have been widely explored as novel optical nanoprobes in biomedical imaging.[7–14] Compared with traditional fluorescence imaging using organic dyes or quantum dots (QDs), the NIR-light-excited upconversion luminescence (UCL) imaging relying on UCNPs exhibits improved tissue penetration depth, uses particles with higher photochemical stability, and is free of auto-fluorescence. Thus it affords remarkably improved in vivo sensitivity .[9] UCNPs could be further engineered to acquire additional functionalities. Gold nanoparticles grown on the surface of the UCNPs can rationally modulate the upconversion emission of nanoparticles.[15] Photosensitizers or chemotherapy drugs may be loaded on UCNPs for dual imaging and therapy applications.[10,16] By introducing Gd^{3+} in the synthesis of UCNPs, multimodal UCL and T_1-weighted MR nanoprobes have been developed.[17–19] The binding of UCNPs with superparamagnetic

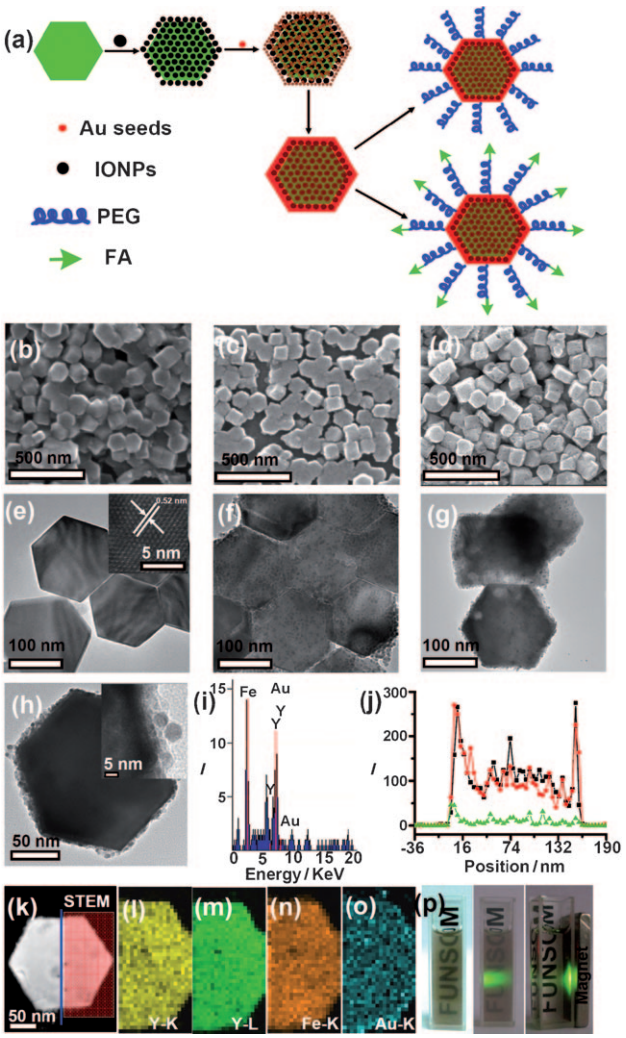

Figure 1. MFNP synthesis and characterization. a) Strategy for MFNP synthesis and functionalization. b–d) SEM images of the UCNPs (b), UCNP–IONP nanocomposites (c), and UCNP-IONP-Au MFNPs (d). e–g) TEM images of UCNPs (e), the inset shows the HRTEM image of a MFNP and the indicated *d* spacing is 0.52 nm; UCNP–IONP nanocomposites (f); and MFNPs (g). h) A TEM image of a single MFNP with high magnification. Inset is a high-resolution (HR) TEM image showing the edge of this MFNP. i) EDS of the MFNPs under the STEM pattern. j, k) A STEM image of a single MFNP (k) and the cross-sectional compositional line profile (j). ■ Y L edge, ● Fe L edge, ▲ Au K edge. l–o) HAADF–STEM–EDS mapping images of an MFNP showing the yttrium K edge (l, yellow), yttrium L edge (m, green), iron K edge (n, orange), and gold K edge (o, blue). p) Photos of a PEG-coated MFNP sample in an aqueous solution under ambient light (left), exposed to a 980 nm laser (middle), and with a neighboring magnet (right).

[*] L. Cheng, K. Yang, C. Wang, Prof. M. Shao, Prof. Z. Liu
Jiangsu Key Laboratory for Carbon-Based Functional Materials & Devices, Institute of Functional Nano & Soft Materials (FUNSOM)
Soochow University, Suzhou, Jiangsu 215123 (China)
E-mail: zliu@suda.edu.cn
mwshao@suda.edu.cn
Dr. Y. Li, Dr. J. Chen
Department of Radiology, the First Affiliated Hospital of Soochow University, Suzhou, Jiangsu 215006 (China)
Prof. S.-T. Lee
Center of Super-Diamond and Advanced Films (COSDAF) and Department of Physics and Materials Science, City University of Hong Kong, Hong Kong SAR (China)

[**] This work was partially supported by the National Natural Science Foundation of China (51002100, 51072126), a National "973" Program of China (2011CB911002), a project funded by the Priority Academic Program Development of Jiangsu Higher Education Institutions, and Research Grants Council of Hong Kong SAR-CRF Grant (CityU5/CRF/08). L.C. was supported by the Innovation Program of Graduate Students in Jiangsu Province (CX10B_036Z). We thank the Molecular Imaging Laboratory at Southeast University of China for their help in MR imaging.

Supporting information for this article is available on the WWW under http://dx.doi.org/10.1002/anie.201101447.

nanoparticles has also been reported, but imaging data were not presented in these studies.[20,21]

Herein, we describe a novel class of multifunctional nanoparticles (MFNPs) based on UCNPs with combined optical and magnetic properties useful in multimodality imaging. The MFNPs were prepared by layer-by-layer (LBL) self-assembly. Ultrasmall superparamagnetic iron oxide (Fe_3O_4) nanoparticles (IONPs) are adsorbed on the surface of a $NaYF_4$-based UCNP by electrostatic attraction to form a UCNP–IONP complex, on top of which a thin gold shell is formed by seed-induced reduction growth (Figure 1 a). The layer of IONPs between UCNPs and the Au shell not only affords MFNPs magnetic properties but also significantly reduces the luminescence quenching effects of the gold nanostructure to UCNPs. The UCNP–IONP–Au MFNPs are then coated by poly(ethylene glycol) (PEG) to impart stability in physiological solutions used for in vitro targeted UCL, MR, and dark-field light scattering imaging. The surface plasmon resonance absorption contributed by the gold shell in MFNPs is utilized for dual-targeted photothermal ablation of cancer cells. In vivo UCL/MR dual-modal imaging with MFNPs was further demonstrated in animal imaging experiments. The composite MFNPs presented herein may have great potential for applications in multimodality biomedical imaging and therapy.

Monodispersed hexagonal $NaYF_4$-based UCNPs (Y/Yb/Er = 69:30:1) were synthesized and coated with poly(acrylic acid) (PAA) according to literature protocols and used as substrates to fabricate multifunctional nanostructures.[5,22,23] Scanning electronic microscopy (SEM) and transmission electronic microscopy (TEM) images revealed that our UCNPs were monodispersed hexagonal nanocrystals with an average diameter of approximately 160 nm (Figure 1 b, e, Supporting Information Figure S1). Ultrasmall superparamagnetic IONPs an average diameter of 5 nm were synthesized by a classical procedure[24] and transferred into the aqueous phase by surface modification with dopamine (DA, Supporting Information Figure S2).

To obtain UCNP–IONP–Au MFNPs, we first mixed different concentrations of DA-modified IONPs with PAA-coated UCNPs for 3 h under constant shaking. Excess unattached IONPs were removed by centrifugation and washing. The zeta potentials of UCNP–IONP nanocomposites increased from −16 to +13 mV with the addition of IONPs (Supporting Figure S3), thus indicating the increase of IONP loading on UCNPs, which was also evidenced by SEM and TEM images (Figure 1 c, f, Supporting Information Figure S4 a, b). UCNP–IONP composite nanoparticles with the highest possible IONP loading were chosen for further Au coating. Negatively charged Au seeds grown in aqueous NaOH[15] were added in large excess and attached to the surface of UCNP–IONP nanocomposites, decreasing the zeta potentials from +13 to −8.5 mV (Supporting Information Figure S3). After removal of unattached gold seeds, a Au shell was grown on the surface of the UCNP–IONPs by seed-mediated reduction of $HAuCl_4$. The thickness of the Au shell was controlled by the volume of the added $HAuCl_4$ growth solution. Representative SEM and TEM images (Figure 1 d, g, Supporting Information Figure S4 c, d) revealed the successful preparation of the UCNP–IONP–Au MFNPs. The line profiles of the elemental composition determined by energy-dispersive X-ray spectroscopy (EDS, Figure 1 i, j) and the elemental mapping in the high-angle annular dark-field scanning TEM (HAADF–STEM) image further evidenced the multicomposite nanostructure with uniformly distributed Y, Fe, and Au elements in one nanoparticle (Figure 1 k–o). The as-prepared MFNPs were then functionalized by PEG through gold-thiol bonds to improve their

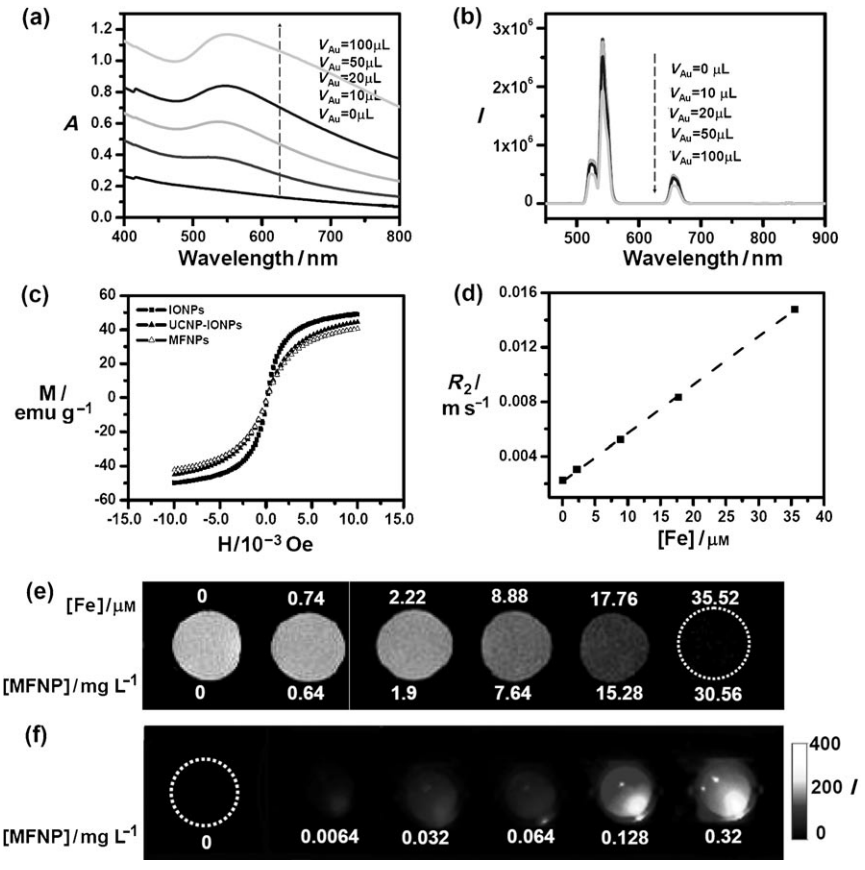

Figure 2. Optical and magnetic properties of MFNPs. a) UV/Vis/NIR absorption spectra of MFNP nanocomposites prepared by adding different volumes of gold growth solutions (V_{Au} = 0, 10, 20, 50, 100 μL). b) The corresponding UCL spectra. c) Magnetization versus magnetic field plots for MFNPs, UCNP–IONP composite, and IONPs at room temperature. d) The T_2 relaxation rates (r_2) of PEG–MFNPs at different Fe concentrations. e) T_2-weighted MR images of PEG–MFNP aqueous solutions at different concentrations. f) UCL images of PEG–MFNP solutions at different concentrations obtained by the Maestro in vivo imaging system. The non-uniformity in the UCL images was due to the shadow of the plate-well wall.

water solubility. PEG-ylated MFNPs with a hydrodynamic diameter of approximately 230 nm were deep purple in color and showed excellent stability in physiological solutions (Figure 1p and Supporting Information Figures S5–S7).

UV/Vis/NIR spectra of MFNPs displayed an absorption peak around 540 nm. An increasing degree of gold coating led to a slight red shift of this band together with the appearance of a continuous absorption band from the visible to NIR regions (Figure 2a), consistent with reports on similar Au-shelled nanostructures.[15,25] The UCL emission of MFNPs was substantially quenched by the gold shell (Figure 2b). MFNPs with approximately 10% UCL quenching and strong optical absorption (prepared by adding 50 μL of 10 mg mL^{-1} $HAuCl_4$ to 5 mL of 0.1 mg mL^{-1} UCNP–IONPs in water) were chosen for further experiments (also selected for representative EM characterization in Figure 1d,g,h–o). The Y/Fe/Au molar ratio was measured by inductively coupled plasma atomic emission spectroscopy (ICP-AES) to be 100:37:4 (Au content 3.4 wt%) in this formulation of MFNPs, corresponding to a rather thin gold shell (thickness ca. 2–3 nm) on the outer surface, as evidenced by HRTEM images (Figure 1h, Supporting Information Figure S8).

The gold coating procedure used herein was adapted from a previous report,[15] in which the Au shell was directly grown on the surface of polymer-coated UCNPs and greatly suppressed their upconversion luminescence. By preventing the direct contact between the UCNP surface and the gold shell, the layer of IONPs in our MFNP composite minimized gold-induced UCL quenching. To confirm our hypothesis, we followed the previous protocol and synthesized a UCNP–Au system by directly growing an Au shell on positively charged UCNPs (Supporting Information, Figure S9). Under the same gold-coating conditions, MFNPs with embedded IONPs showed significantly reduced quenching compared to the UCNP–Au system (Supporting Information Figure S10). Our data demonstrated the unique roles of IONPs in this MFNP system, as both the MR imaging contrast agent and also the "buffer" to reduce the quenching effect of the gold shell to UCNPs; the latter role is similar to that of the PEG polymer coating in a quantum dot–Au shell system reported by Gao and coworkers.[1]

The magnetic properties of the MFNPs were evaluated by the field-dependent magnetization measurements (Figure 2c). The absence of a hysteresis loop suggested the superparamagnetic nature of our MFNPs. T_2-weighted MR images of PEG-ylated MFNPs acquired on a 7 T MR scanner revealed the concentration-dependent darkening effect, showing a high transverse relaxivity (r_2) of our MFNPs of 352.8 mM^{-1} s^{-1} (Figure 2d). Aqueous solutions of MFNPs were also imaged by the Maestro in vivo optical imaging system using a 980 nm NIR laser as the excitation source (Figure 2f). Even at an MFNP concentration as low as 6.4 μg L^{-1}, the UCL signals could still be detected. While optical imaging provides a much higher imaging sensitivity, MR imaging is not limited by the tissue penetration depth and is able to image targets located deep inside the body.

We next used MFNPs for in vitro cell imaging. Standard cell toxicity tests revealed no obvious toxic effect of our PEG-ylated MFNPs to treated cells at concentrations below 1 mg mL^{-1} (Supporting Information Figure S11). As a demonstration, folic acid (FA) was conjugated to MFNPs through a PEG linker to target the folate receptor (FR), which is widely known to be up-regulated in many types of cancer cells. FR-positive human epidermoid carcinoma KB cells cultured in an FA-free medium and FR-negative HeLa cells cultured in a normal medium were incubated with PEG–MFNP or FA–PEG–MFNP (0.05 mg mL^{-1}) for confocal UCL imaging with 980 nm excitation (Figure 3a,b). Strong UCL signals were observed for KB cells incubated with FA–PEG–MFNP, while cells incubated with PEG–MFNP showed negligible nonspecific binding. No obvious UCL signal was noted from HeLa cells (FR−) after incubation with either FA–PEG–MFNP or PEG–MFNP. The FR blocking experi-

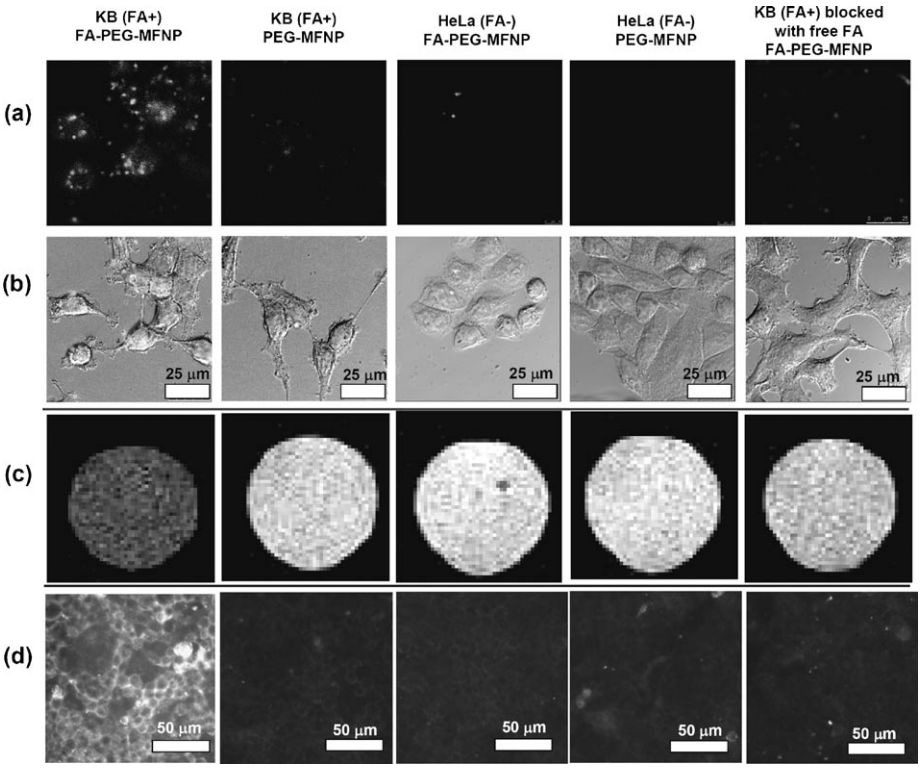

Figure 3. Multimodal targeted in vitro imaging of cancer cells. a, b) Confocal UCL emission (a) and merged UCL/bright field (b) images of KB or HeLa cells after incubation with FA–PEG–MFNP or PEG–MFNP as indicated. c) T_2-weighted MR images of cancer cells treated with MFNPs. The cells were suspended in 1% agarose gel for MR imaging. d) Dark-field optical microscopy images of the corresponding cancer cell samples. Strong UCL signals, obvious T_2-weighted MR darkening effect, and bright light scattering were observed from KB cells treated with FA–PEG–UCNP but not from other control samples. MFNPs at 0.05 mg were used in the above experiments.

ment further evidenced the highly specific FR targeting by FA–PEG–MFNP.

Both the IONP layer and the gold shell could be utilized in different imaging modalities. After MFNP incubation, cells were transferred into agarose gel pellets and imaged by the 7 T MR scanner. As expected, KB cells incubated with FA-PEG-MFNP showed drastically reduced signals in T_2-weighted MR images compared with other control cells (Figure 3c, Supporting Information Figure S12). Besides UCL emission and MR contrast, MFNPs with gold shells that exhibit strong surface plasmon resonance scattering are useful for dark-field light scattering imaging,[26] showing bright scattered light signals from KB cells incubated with FA-PEG-MFNP but not from other samples (Figure 3d). These results reveal the great potential of our MFNPs for multimodal cancer cell labeling and imaging.

Gold nanostructures possess surface plasmon absorption with large cross sections and have been widely used in photothermal therapies (PTT).[27–30] Our MFNPs containing gold shells also exhibited a wide absorption band from the visible to the NIR region. When exposed to an 808 nm NIR laser at a power density of 1 $W cm^{-2}$ (Figure 4a), the temperature of the MFNP solution increased from approximately 20 to 50 °C in 5 min, in marked contrast to the small temperature changes of the irradiated water and the UCNP–IONP sample. The photothermal effect of MFNPs was then used for targeted PTT of cancer cells. KB cells were incubated with FA–PEG–MFNP or PEG–MFNP (0.05 mg mL^{-1}) for 30 min, washed to remove nanoparticles, reincubated for 2 h, and then exposed to an 808 nm laser at a power density of 1 $W cm^{-2}$ for 5 min. The majority of KB cells treated by FA–PEG–MFNP were killed after laser irradiation (Figure 4b), while untreated and PEG–MFNP treated cells showed either negligible cell death or much less cell death after exposure to the NIR laser (Supporting Information Figure S13). Besides molecular targeting, the magnetic properties of MFNPs can also be taken advantage of for magnetic targeted PTT.[2,31] HeLa cells were incubated with PEG–MFNP for 2 h at 37 °C in the presence of a magnetic field. After the cells were washed to remove free nanoparticles, UCL imaging revealed the highly enhanced uptake of MFNPs for cells close to the magnet (Figure 4c). After being exposed to the NIR laser for 5 min, cells near the magnet were effective destructed, while those far from the magnet were essentially unaffected (Figure 4d–j). These results clearly demonstrate the unique molecular/magnetic dual-targeted cancer PTT using our MFNPs.

The capability of MFNPs as multimodal imaging probes was further evidenced in vivo. Female nude mice bearing KB human epidermoid carcinoma tumors were intravenously injected with PEG–MFNP (160 μL of 2.5 mg mL^{-1} solution for each mouse), and then imaged by the Maestro in vivo imaging system (CRi Inc.). The UCL emission at 660 nm from MFNPs was collected for in vivo imaging. Strong UCL signals from the liver and tumor sites were observed one hour after intravenous injection, suggesting high liver and tumor uptake of MFNPs (Figure 5a–c, Supporting Information Figure S14a). Ex vivo UCL imaging of organs collected from mice 24 h post injection of MFNPs revealed the high accumulation of MFNPs in the tumor and reticuloendothelial systems (RES), including liver, spleen, lung, and bone marrow, without appreciable signals from other tissues (Figure 5d, Supporting Information Figure S14b). T_2-weighted MR imaging was also conducted after intravenous injection of MFNPs, showing obvious darkening effects in the liver and tumor after injection, with MR signals decreased by 45.4 and 38.6%, respectively (Figure 5e,f, Supporting Information, Figure S15). Images of Prussian blue stained tissue slices further confirmed the accumulation of MFNPs in the tumor and RES organs (Supporting Information Figure S16). The

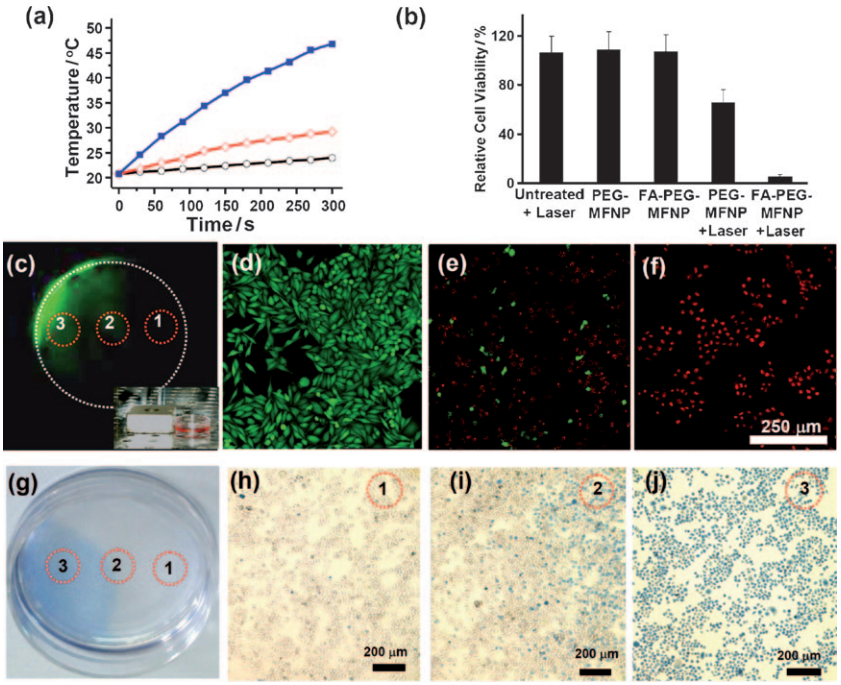

Figure 4. Dual-targeted photothermal ablation of cancer cells. a) The heating curves of water (○), UCNP–IONP (1 mg mL^{-1}) nanocomposite (◇), and MFNP (■, 1 mg mL^{-1} in total, or 0.034 mg mL^{-1} by Au content) under 808 nm laser irradiation at a power density of 1 $W cm^{-2}$. b) Relative viabilities of PEG–MFNP or FA–PEG–MFNP treated KB cells with or without laser irradiation (808 nm, 1 $W cm^{-2}$, 5 min). c) A UCL image of HeLa cells in a culture dish after incubation with PEG–MFNP in the presence of magnetic field taken by the Maestro in vivo imaging system (980 nm excitation). Inset: a photo showing the experimental set-up. A magnet was placed close to the cell culture dish. d–f) Confocal images of calcein AM (green, live cells) and propidium iodide (red, dead cells) co-stained cells after magnetic targeted PTT. Images were taken at different locations in the culture dish: 1) far from the magnet (d), 2) in the middle (e), and 3) close to the magnet (f). g) A digital photo of the cell culture dish after magnetic targeted PTT and trypan blue staining. h–j) Optical microscopy images of trypan blue stained cells after magnetic targeted PTT. Images were taken at different locations in the culture dish: 1) far from magnet (e), 2) in the middle (f), and 3) close to the magnet (g). MFNPs at 0.05 mg mL^{-1} were used in the above in vitro experiments.

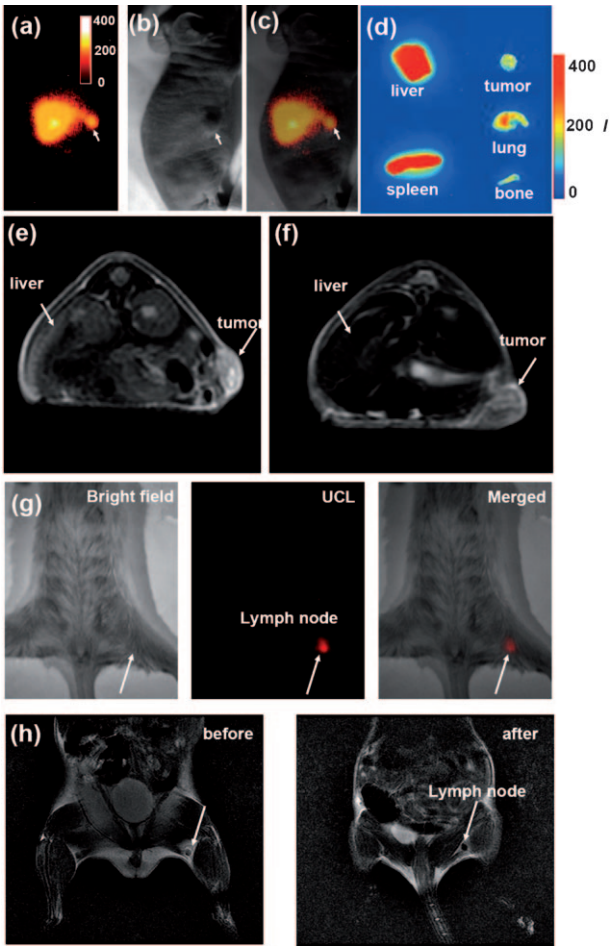

Figure 5. Dual-modal UCL/MR in vivo imaging. a–c) The bright field (a), UCL (b), and merged (c) images of a KB tumor-bearing mouse one hour after intravenous injection of PEG–MFNP. Strong UCL signals were observed from the liver and tumor sites (arrow) of the mouse. d) Ex vivo UCL imaging showing accumulation of MNFPs in the liver, spleen, tumor, bone, and lung of the injected mouse at 24 h post injection. UCL signals from other organs were barely detectable. e, f) T_2-weighted images of KB-tumor bearing nude mice with (e) and without (f) injection of MFNPs. Obvious darkening contrast was shown in the mouse liver and tumor. g, h) Multimodal UCL (g) and MR (h) imaging for in vivo lymphangiography mapping using MFNPs. MR images were taken before (left) and after (right) injection of MFNPs.

tumor passive uptake of MFNP nanoparticles is likely due to the enhanced permeability and retention (EPR) effect of cancerous tumors and may be utilized for in vivo imaging-guided photothermal/magnetic hyperthermia ablation of tumors in the future.

Finally, MFNPs were also used for multimodal mapping of lymph nodes in mice. As local lymphatic drainage is an important route for the metastasis of cancer cells, identification of the sentinel lymph nodes has become a common staging procedure for cancers.[9,32] We intracutaneously injected PEG–MFNPs (15 μL, 2.5 mg mL^{-1}) into one rear paw of a mouse to monitor the lymphatic drainages in the lower trunk. The primary lymph node to which MFNPs migrated by lymphatic drainage was visualized by in vivo UCL imaging two hours after injection (Figure 5g, Supporting Information Figure S17). The dark spot observed in MR images was also unambiguously assigned to the brachial lymph node on the basis of the detailed anatomical information provided by MRI (Figure 5h, Supporting Information Figure S15).

In summary, MFNPs based on UCNPs with combined optical and magnetic properties are synthesized via a simple LBL self-assembly strategy. PEG-ylated MFNPs can be used for in vitro targeted UCL, MR, and dark-field imaging; for molecular and magnetic targeted PTT of cancer cells; and as a contrast agent for in vivo dual-modal UCL/MR imaging in mice. Our work shows a facile method to prepare a novel class of multimodality imaging nanoprobes with a wide range of useful functionalities. The UCNP is the core and substrate of this MFNP system and offers UCL emission for optical imaging. IONPs afford the nanocomposites superparamagnetic properties useful in T_2-weighted MR imaging and magnetic targeted therapy and also serve as a "buffer" layer between the luminescent UCNP core and the outside gold shell to reduce the UCL quenching effect. The gold shell grown on top of the IONP layer allows easy chemical functionalization of MFNPs through the widely applied gold–thiol chemistry and also exhibits surface plasmon resonance in the visible and NIR regions, which can be utilized in PTT and dark-field scattering imaging as well as possibly for photoacoustic and Raman imaging.[33,34] The multimodal UCL optical/MR imaging could combine the advantages of each single imaging tool for enhanced sensitivity and improved tissue penetration. The dual molecular/magnetic targeting may allow more selective and localized therapies. Although further work may be needed to optimize their sizes and surface coatings for reduced RES uptake, as well as to demonstrate the in vivo molecular targeted imaging and photothermal therapy using MFNPs, the UCNP-based MFNPs developed herein are promising for many applications in biomedicine, including multimodality imaging, cell tracking, and imaging-guided novel targeted cancer therapies.

Received: February 27, 2011
Revised: April 27, 2011
Published online: June 28, 2011

Keywords: imaging agents · multifunctional systems · nanoparticles · photothermal therapy · upconversion

[1] Y. Jin, X. Gao, *Nat. Nanotechnol.* **2009**, *4*, 571.
[2] S.-H. Hu, X. Gao, *J. Am. Chem. Soc.* **2010**, *132*, 7234.
[3] E.-K. Lim, J. Yang, C. P. N. Dinney, J.-S. Suh, Y.-M. Hu, S. Haam, *Biomaterials* **2010**, *31*, 9310.
[4] Y. T. Lim, Y.-W. Noh, J.-H. Cho, J. H. Han, B. S. Choi, J. Kwon, K. S. Hong, A. Gokarna, Y.-H. Cho, B. H. Chung, *J. Am. Chem. Soc.* **2009**, *131*, 17145.
[5] H. Mai, Y. Zhang, R. Si, Z. Yan, L. Sun, L. You, C. Yan, *J. Am. Chem. Soc.* **2006**, *128*, 6426.
[6] L. Wang, R. Yan, Z. Huo, L. Wang, J. Zeng, J. Bao, X. Wang, Q. Peng, Y. Li, *Angew. Chem.* **2005**, *117*, 6208; *Angew. Chem. Int. Ed.* **2005**, *44*, 6054.
[7] X. Yu, M. Li, M. Xie, L. Chen, Y. Li, Q. Wang, *Nano Res.* **2010**, *3*, 51.

[8] D. K. Chatterjee, M. K. Gnanasammandhan, Y. Zhang, *Small* **2010**, *6*, 2781 – 2795.
[9] L. Cheng, K. Yang, S. Zhang, M. Shao, S. Lee, *Nano Res.* **2010**, *3*, 722.
[10] C. Wang, L. Cheng, Z. Liu, *Biomaterials* **2011**, *32*, 1110.
[11] M. Nyk, R. Kumar, T. Y. Ohulchanskyy, E. J. Bergey, P. N. Prasad, *Nano Lett.* **2008**, *8*, 3834.
[12] L. Xiong, Z. Chen, Q. Tian, T. Cao, C. Xu, F. Li, *Anal. Chem.* **2009**, *81*, 8687.
[13] X.-F. Yu, Z. Sun, M. Li, Y. Xiang, Q.-Q. Wang, F. Tang, Y. Wu, Z. Cao, W. Lia, *Biomaterials* **2010**, *31*, 8724.
[14] L. Cheng, K. Yang, M. Shao, S.-T. Lee, Z. Liu, *J. Phys. Chem. C* **2011**, *115*, 2686.
[15] H. Zhang, Y. Li, I. A. Ivanov, Y. Qu, Y. Huang, X. Duan, *Angew. Chem.* **2010**, *122*, 2927; *Angew. Chem. Int. Ed.* **2010**, *49*, 2865.
[16] H. S. Qian, H. C. Guo, P. C.-L. Ho, R. Mahendran, Y. Zhang, *Small* **2009**, *5*, 2285.
[17] Y. I. Park, J. H. Kim, K. T. Lee, K.-S. Jeon, H. B. Na, J. H. Yu, H. M. Kim, N. Lee, S. H. Choi, S.-I. Baik, H. Kim, S. P. Park, B.-J. Park, Y. W. Kim, S. H. Lee, S.-Y. Yoon, I. C. Song, W. K. Moon, Y. D. Suh, T. Hyeon, *Adv. Mater.* **2009**, *21*, 4467.
[18] J. Zhou, Y. Sun, X. Du, L. Xiong, H. Hua, F. Li, *Biomaterials* **2010**, *31*, 3287.
[19] J. Zhou, M. Yu, Y. Sun, X. Zhang, X. Zhu, Z. Wu, D. Wu, F. Li, *Biomaterials* **2011**, *32*, 1148.
[20] J. Shen, L.-D. Sun, Y.-W. Zhang, C.-H. Yan, *Chem. Commun.* **2010**, *46*, 5731.
[21] C. Mi, J. Zhang, H. Gao, X. Wu, M. Wang, Y. Wu, Y. Di, Z. Xu, C. Mao, S. Xu, *Nanoscale* **2010**, *2*, 1141.
[22] G. S. Yi, G. M. Chow, *Adv. Funct. Mater.* **2006**, *16*, 2324.
[23] F. Wang, X. Liu, *J. Am. Chem. Soc.* **2008**, *130*, 5642.
[24] S. Sun, H. Zeng, D. B. Robinson, S. Raoux, P. M. Rice, S. X. Wang, G. Li, *J. Am. Chem. Soc.* **2004**, *126*, 273.
[25] Y. Chen, H. Chen, D. Zeng, Y. Tian, F. Chen, J. Feng, J. Shi, *ACS NANO* **2010**, *4*, 6001.
[26] I. H. El-Sayed, X. Huang, M. A. El-Sayed, *Nano Lett.* **2005**, *5*, 829.
[27] G. von Maltzahn, J.-H. Park, A. Agrawal, N. K. Bandaru, S. K. Das, M. J. Sailor, S. N. Bhatia, *Cancer Res.* **2009**, *69*, 3892.
[28] H. Liu, D. Chen, L. Li, T. Liu, L. Tan, X. Wu, F. Tang, *Angew. Chem.* **2011**, *123*, 921; *Angew. Chem. Int. Ed.* **2011**, *50*, 891.
[29] S. E. Skrabalak, J. Chen, Y. Sun, X. Lu, L. Au, C. M. Cobley, Y. Xia, *Acc. Chem. Res.* **2008**, *41*, 1587.
[30] M. Hu, J. Chen, Z.-Y. Li, L. Au, G. V. Hartland, X. Li, M. Marquez, Y. Xia, *Chem. Soc. Rev.* **2006**, *35*, 1084.
[31] J. Kim, S. Park, J. E. Lee, S. M. Jin, J. H. Lee, I. S. Lee, I. Yang, J.-S. Kim, S. K. Kim, M.-H. Cho, T. Hyeon, *Angew. Chem.* **2006**, *118*, 7918; *Angew. Chem. Int. Ed.* **2006**, *45*, 7754.
[32] H. Kobayashi, Y. Koyama, T. Barrett, Y. Hama, C. A. S. Regino, I. S. Shin, B.-S. Jang, N. Le, C. H. Paik, P. L. Choyke, Y. Urano, *ACS Nano* **2007**, *1*, 258.
[33] X. Qian, X.-H. Peng, D. O. Ansari, Q. Yin-Goen, G. Z. Chen, D. M. Shin, L. Yang, A. N. Young, M. D. Wang, S. Nie, *Nat. Biotechnol.* **2008**, *26*, 83.
[34] X. Yang, S. E. Skrabalak, Z.-Y. Li, Y. Xia, L. V. Wang, *Nano Lett.* **2007**, *7*, 3798.

